Advancing PPG-Based Continuous Blood Pressure Monitoring from a Generative Perspective

Hui Ji
University of Pittsburgh
Pittsburgh, USA
huj16@pitt.edu

Pengfei Zhou
University of Pittsburgh
Pittsburgh, USA
pengfeizhou@pitt.edu

ABSTRACT

Cuffless blood pressure (BP) monitoring is a critical task in the cardiovascular diseases (CVDs) domain, commonly based on Photoplethysmography (PPG) and Electrocardiogram (ECG) signals, providing foresight into cardiac health. While ECG often delivers better BP monitoring performance, the acquisition via straps and patches leads to a poor user experience. On the contrary, PPG enables continuous and convenient monitoring, but offers less informative references. A potential approach is to convert PPG signals into ECG signals, ensuring both high convenience and optimal accuracy. Converting PPG into ECG, however, involves a substantial reduction in inherent entropy, necessitating a thorough understanding of the process and specific techniques to guide the ECG generation. In this paper, we present a blood pressure monitoring framework that achieves ECG-level performance using solely the PPG signal. A diffusion model is introduced to conduct a selective ECG-targeted generative process with the condition of PPG. Based on our observation from the experimental investigation, a set of techniques is developed to significantly enhance the model's ability in generating high-quality ECG signals. Specifically, in the forward process, we employ an adaptive search module to adapt the QRS segment within the ECG waveform. In the reverse process, we propose the scale alignment and frequency alignment modules to better guide the generative process. Extensive experiments conducted on two public datasets and one self-collected dataset demonstrate the superior performance of our proposed framework, offering a groundbreaking perspective for PPG-based continuous blood pressure monitoring.

CCS CONCEPTS

• **Applied computing** → **Health informatics**; • **Computing methodologies** → **Machine learning approaches**; **Modeling and simulation**; • **General and reference** → **Estimation**.

KEYWORDS

Continuous Blood Pressure Monitoring, PPG, Diffusion Model, ECG Generation

SENSYS '24, November 4–7, 2024, Hangzhou, China

ACM ISBN 979-8-4007-0697-4/24/11.
https://doi.org/10.1145/3666025.3699365

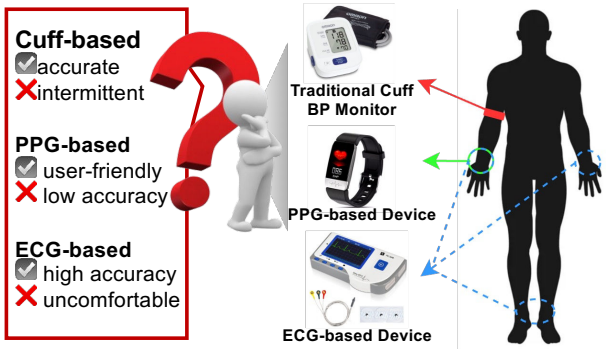

Figure 1: Different blood pressure measuring devices and corresponding advantages and disadvantages.

ACM Reference Format:
Hui Ji and Pengfei Zhou. 2024. Advancing PPG-Based Continuous Blood Pressure Monitoring from a Generative Perspective. In *The 22nd ACM Conference on Embedded Networked Sensor Systems (SENSYS '24), November 4–7, 2024, Hangzhou, China.* ACM, New York, NY, USA, 14 pages. https://doi.org/10.1145/3666025.3699365

1 INTRODUCTION

As the leading risk factor of cardiovascular diseases (CVDs) [40], hypertension has been commonly used as the critical criterion for diagnosis and prevention. Consequently, precisely and continuously monitoring blood pressure (BP) throughout individuals' daily routines becomes imperative to facilitate early detection and intervention for CVDs. Several categories of approaches have been applied to monitor BP, as shown in Figure 1, where there are three types of devices: traditional cuff BP monitors, Photoplethysmography (PPG)-based devices, and Electrocardiogram (ECG)-based devices. The cuff-based BP monitoring device operates via cuffs, making them cumbersome, inconvenient, and limited to episodic readings. For a long time, ECG has been the gold standard [28, 38, 72] for cuffless BP monitoring, providing crucial insights into diagnosing numerous CVDs. However, their reliance on specialized equipment and the method of acquisition involving straps and patches have constrained their accessibility and affordability for monitoring daily cardiac activities. In order to address these constraints, Photoplethysmography (PPG) has emerged as a promising alternative, due to its non-invasive, cost-effective and easy-to-integrate characteristics, for continuous blood pressure monitoring in wrist-worn wearable devices. Nonetheless, compared to ECG, PPG measures blood volume changes but lacks the detailed cardiac insights of ECG, limiting its use in CVDs.

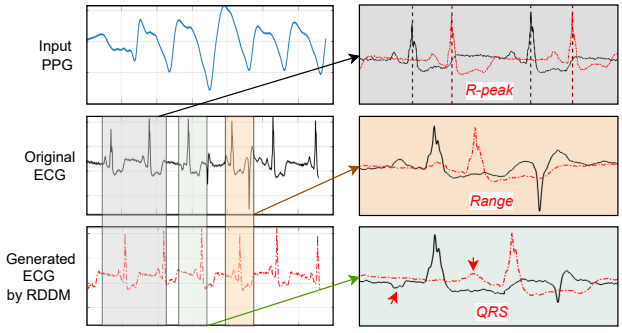

Figure 2: The ECG generated by RDDM exhibits limitations in signal fidelity: misalignment of R-Peak, variability in amplitude, and distortions in QRS waveform.

This paper is motivated by an essential question: *is it feasible to achieve ECG-level performance for blood pressure monitoring using only the low-cost and convenient PPG signal?* To harness the convenience of PPG monitoring alongside the diagnostic utility of ECG [63], PPG-to-ECG conversion has emerged as a promising albeit challenging alternative [64]. Previous generative models [65, 69, 80], however, fail to effectively manage the substantial entropy reduction in the generative process, leading to a lack of guidance in aligning key features between the signals and, consequently, to unsatisfactory model performance. Despite commendable progress, there still exist significant performance disparities when incorporating the generated ECG in BP estimation tasks compared to utilizing the original ECG directly.

In this paper, we first investigate the reasons why existing generative models fail to produce high-quality ECG signals using only PPG as inputs. The Region-Disentangled Diffusion Model (RDDM) [69] is the state-of-the-art diffusion model for PPG to ECG conversion. It makes a minor modification to the basic diffusion model by introducing a region of interest (ROI)-guided forward process, where it employs a fixed window size to locate QRS regions. Figure 2 illustrates the performance of RDDM in generating the ECG signal with the PTT-PPG dataset [45]. The ECG signal is primarily comprised of three components: the P wave, the QRS complex, and the T wave. The P wave represents atrial depolarization, the QRS complex indicates ventricular depolarization, and the T wave reflects ventricular repolarization. As depicted in Figure 2, significant discrepancies in R-peak, amplitude range, and QRS complex are observed between the original ECG and the generated one by RDDM. In detail, the failure of the R-peak reconstruction is primarily due to the scale misalignment. The original R-peak is distinct and sharp, while the generated R-peak is misaligned, potentially leading to misidentification of heartbeat timing. Meanwhile, RDDM does not generate the correct amplitude range of the ECG signal, as indicated by the highlighted area. Accurate amplitude representation is essential for assessing the signal's overall quality. Additionally, RDDM fails to accurately reproduce the shape and amplitude characteristics of the original QRS complex, which are crucial for identifying heartbeats. These observations suggest that the simple enhancement made by RDDM to the basic diffusion model is insufficient to address the complexities involved in ECG generation. It struggles with preserving critical details such as the R-peaks, signal amplitude range, and QRS complex. These deficiencies impair the model's effectiveness in consistently and accurately monitoring BP situations that require precise ECG signal interpretation.

Recognizing the significance of local details in the generated ECG waveform for continuous BP monitoring, we propose a PPG-conditional Generative model-based framework (PPGG) to enhance continuous blood pressure monitoring. In the forward process, we develop a QRS adaptive search module to locate the QRS complex so that we can selectively add noise to specific regions of interest (QRS or non-QRS) in the ECG and align them in the generation process. This approach avoids the inaccuracies associated with fixed windows and provides a potential alignment constraint for more targeted ECG generation in the subsequent reverse process. In the reverse process, the decoder denoises both QRS and non-QRS regions under a PPG condition. It is worth noting that we abandon the fixed QRS region localization approach, opting instead for adaptive localization along signal variations. In particular, based on our unique findings, except for the alignment of QRS complex, we design alignment modules for both scale-wise and frequency-wise features, enabling capturing complex temporal dynamics and frequency intricacies of ECG signals to improve the generation quality. Additionally, we design a BiLSTM-based BP estimator, which processes information in both forward and backward directions. This method is better at capturing the crucial influences of preceding and subsequent signals on blood pressure than simple feedforward networks like U-Net. Finally, our end-to-end framework incorporates the blood pressure estimation loss into the training process, ensuring that the model directly optimizes blood pressure prediction alongside ECG generation.

We conduct extensive experiments based on two public datasets and one self-collected dataset in real-world scenarios. We comprehensively evaluate the effectiveness of our proposed PPGG framework and compare it with multiple baselines and state-of-the-art (SOTA) models. The results indicate that PPGG significantly outperforms SOTA models. On average, it reduces the MAE by 36.5% for SBP estimation and 28.1% for DBP estimation, respectively. In the PTT-PPG dataset, the ECG signal generated by PPGG surprisingly outperforms the original ECG signal in BP estimation. The real-world experiments using the self-collected dataset demonstrate the effectiveness of PPGG over a continuous three-day period, suggesting its potential for long-term continuous blood pressure monitoring in real-life scenarios.

Our main contributions are summarized as follows:

- We observed the unsatisfactory performance of generating ECG from PPG using SOTA models, and identified the major reasons behind. They fail to account for the inherent entropy-reducing nature of the PPG-to-ECG transformation, leading to poor alignment of key features and inaccurate estimation.
- We propose PPGG, a novel PPG-based generative framework, which reconstructs the ECG signal with PPG condition, specifically for BP monitoring. To the best of our knowledge, this is the first end-to-end diffusion model-based framework for BP monitoring.

- We design a set of techniques to guide the entropy-reducing process in generating the ECG for BP monitoring. In the forward process, we employ a QRS adaptive search module to adapt the QRS segment within the ECG waveform. In the reverse process, we propose the scale and frequency alignment modules. In the former, we ensure the alignment of the R-peak position and the signal amplitude range; in the latter, the consistency of the R-peck frequency is guaranteed. We adopt a BiLSTM-based BP estimator to capture the key temporal dependencies in the blood pressure signal. Additionally, our end-to-end framework integrates blood pressure estimation loss, optimizing the model for precise blood pressure estimation concurrent with ECG generation.
- Comprehensive experiments are conducted based on two popular datasets to evaluate the quality of the generated ECG for BP estimation. We also validate the model's practical applicability over a continuous three-day period through a real-world case study.

The rest of this paper is organized as follows: Section 2 presents the background and motivation. In Section 3, we introduce the proposed model, detailing its components and theoretical foundations. Section 4 describes the experimental setup, including the datasets, data pre-processing, and evaluation metrics used to evaluate the model. Section 5 discusses the results and provides an in-depth analysis of the findings. Section 6 reviews related work, situating our research within the existing literature. Finally, Section 7 concludes the paper by summarizing the key points and suggesting future research directions.

2 BACKGROUND AND MOTIVATION

2.1 Classic Blood Pressure Monitoring

Cuff-based methods. Initially, BP measurements [10, 52] were conducted manually by Stephen Hales in 1733 [79], who measured BP by inserting a glass tube into the artery of a horse and then observing the fluctuations of the blood in such tube. The demand for improved user experience has resulted in numerous non-invasive blood BP measurement techniques. The first non-invasive approach was proposed by Scipione Riva-Rocci [76] in 1896 with the invention of the pneumatic cuff. In 1905, Nikolai Korotkoff discovered the Korotkoff sounds, which established the manual auscultatory method still in use today. Oscillometry [9, 46, 60] is another non-invasive and automatic cuff-based method, which is currently the most widely used in clinical practice. The primary limitation of cuff-based BP monitoring lies in its discontinuous nature.

ECG-based methods. The gold standard status of ECG in non-invasive BP monitoring [28, 38, 72] stems from its capacity to serve as a crucial electrical indicator of cardiac activity. The interrelation between segments of the ECG and BP plays a pivotal role in elucidating cardiac mechanics. As shown in Figure 3, the P wave[38, 66], which denotes atrial contraction, indirectly contributes to the enhancement of blood volume during ventricular contraction, potentially leading to a transient rise in systolic blood pressure by promoting adequate ventricular preload. Moreover, the QRS complex [30, 31], signifying ventricular contraction, exerts a direct influence on systolic blood pressure through its attributes such as width and

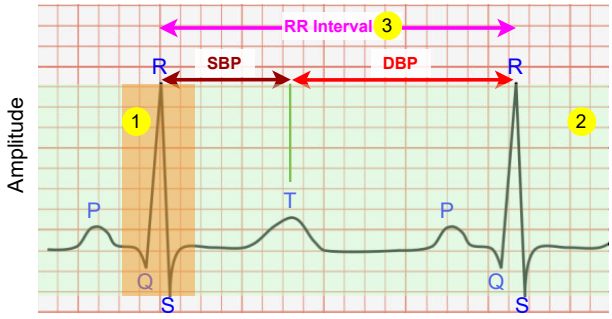

Figure 3: Standard ECG waveform intervals, including RR interval, and their correlations with systolic (SBP) and diastolic blood pressure (DBP).

morphology, denoting the force and rapidity of ventricular contraction. Furthermore, the T wave [31], which marks ventricular relaxation, is vital for cardiac preparation for subsequent filling and contraction cycles. This relaxation phase indirectly modulates diastolic blood pressure, with any abnormalities suggesting potential complications in ventricular relaxation that may impair cardiac output and the regulation of blood pressure. An alternative perspective posits that the amplitude of the R wave [15, 51, 78] may correlate with the contractile force of the left ventricle, while subtle fluctuations in the R-peak could be indicative of autonomic nervous system regulation. This system plays a crucial role in modulating vascular tension, which in turn influences blood pressure. Furthermore, alterations in heart rate [2, 18] are indicative of shifts in blood flow requirements, thereby mirroring variations in blood pressure. The main drawback of ECG-based methods is the uncomfortable user experience.

PPG-based methods. Recently, PPG-based methods [67, 81] are gaining prominence due to their continuous and non-invasive monitoring characteristics, especially the user-friendly experience. PPG [21] measures blood volume changes in the microvascular bed of tissue, providing indirect BP measurements. These techniques benefit from advancements in machine learning and signal processing, enhancing the precision and reliability of BP monitoring. However, compared to ECG signals, PPG signals [81] exhibit a less direct correlation with blood pressure. That is why PPG often has less measurement accuracy than ECG. Even so, PPG-based methods [16, 49] still appeal to many interests from both academia and industry and now many researchers and engineers strive to improve the accuracy of PPG-based methods, aiming to achieve continuous, accurate, and user-friendly BP monitoring for people's daily life.

2.2 Reconstructing ECG for BP Monitoring

ECG contains more detailed information about the heart's electrical activity compared to PPG. Since blood pressure is closely related to the dynamics of cardiac cycles and electrical conduction, ECG signals offer better predictive power for estimating blood pressure.

PPG-to-ECG conversion. Researchers have endeavored to reconstruct the ECG signal from the PPG signal from three main aspects, i.e., Bio-feature-based methods, CNN-based models, and

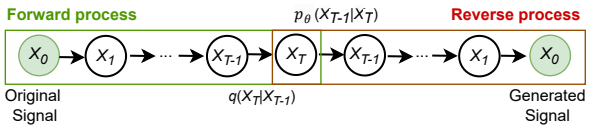

Figure 4: Basic framework of the diffusion model.

generative models for direct conversion. The Bio-feature-based methods [87] fail to capture the nonlinear relationship between the two domains, thereby reducing the quality of ECG reconstruction. CNN-based models [4] normally blindly look for and extract representations in PPG and ECG. However, the lack of contextual information and the limited sensitivity to complex conditions pose insurmountable constraints in practical scenarios. Recently, various generative models have been studied for reconstructing the ECG, including GAN-based [65, 80], Transformer-based [37], and flow-based [69] models. Among these, the flow-based models (diffusion models) show a high potential in reconstructing high-quality ECG signals. However, their performance suffers from degradation and instability in BP monitoring tasks due to a lack of in-depth understanding and proper guidance for the conversion process.

Diffusion model. Figure 4 depicts the basic framework of the diffusion model, which operates in two main processes: the forward process and the reverse process. In the forward process, the original signal X_0 undergoes successive transformations, resulting in increasingly noisy versions $X_1, X_2, \ldots, X_T$. The reverse process then uses the noisy signal X_T to reconstruct the original signal through a series of denoising steps, ultimately generating X_0 from X_T. The transition from X_T to X_{T-1} is modeled by a learned probability distribution $p_\theta(X_{T-1} \mid X_T)$. When a condition containing useful information is added in the reverse process, the system's state space is constrained or simplified, reducing possibilities and randomness, thereby decreasing the system's entropy. Specifically, this condition may provide some prior knowledge or specific constraints, thus reducing the system's degrees of freedom. The diffusion model is designed to iteratively add and remove noise in the data, making them ideal for generating high-quality synthetic signals from noisy or incomplete data. When iteratively adding Gaussian noise in the data, it significantly expands the space to ensure a more complete representation searching. The iterative refinement process helps to model the data more accurately, allowing for a larger and more comprehensive feature space that better captures the nuances of physiological signals.

2.3 Motivation

Experimental investigation. As shown in Figure 2, we observed unsatisfactory ECG reconstruction details utilizing the SOTA diffusion model RDDM [69]. The limitations mainly consist of distortions in the QRS waveform, variability in signal amplitude, and misalignment of R-Peak. To this end, we anticipate that incorporating targeted alignment modules and constraints may address these issues and improve the reconstruction quality. To validate our hypotheses, we conduct two experiments using Amplitude Normalization and Peak Alignment to underscore the importance of ECG waveform details. Figure 5(a) and (b) plot the original ECG signal and the ECG

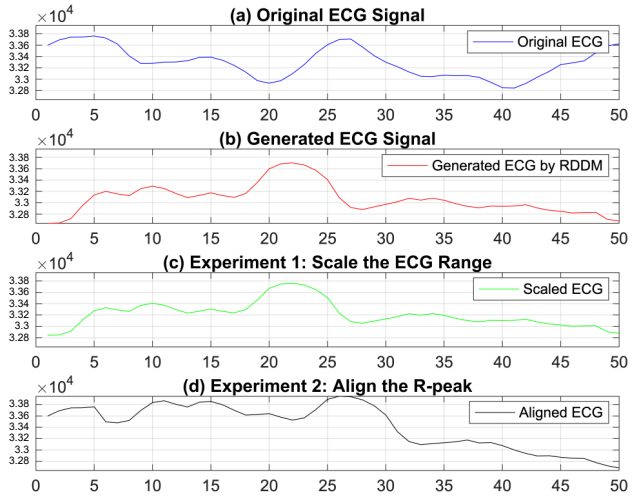

Figure 5: Experimental investigation on the feasibility of incorporating targeted alignment modules and constraints to improve the quality of generated ECG.

signal generated from PPG measurements by RDDM, respectively. In Experiment 1, our objective is to adjust the generated ECG signal so that its maximum and minimum values are close to or equal to those of the original ECG signal. We begin by calculating the maximum and minimum values of both the original and generated ECG. The scaling factor is computed using the formula $\text{scale\_factor} = \frac{\max_{\text{orig}} - \min_{\text{orig}}}{\max_{\text{gen}} - \min_{\text{gen}}}$. This factor is applied to the generated ECG using $\text{ECG\_gen\_scaled} = (\text{ECG\_gen} - \min_{\text{gen}}) \times \text{scale\_factor} + \min_{\text{orig}}$. To validate the results, we re-calculate the maximum and minimum values of the scaled-generated ECG to ensure they match those of the original signal. The result is plotted in Figure 5(c). Experiment 2 aims to align the peaks of the generated ECG with those of the original ECG using the interpolation method to cope with the frequency mismatch. We detect the R-peak positions in both signals and calculate the time differences between each pair of corresponding peaks with $\Delta t_i = t_{\text{orig},i} - t_{\text{gen},i}$. The generated ECG is then adjusted by shifting it in time to align all peaks using interpolation: $\text{ECG\_gen\_aligned}(t) = \text{ECG\_gen}(t - \Delta t)$. Finally, we validate the results by re-detecting the peak positions in the aligned generated signal to confirm that they match the peak positions in the original ECG. The result is plotted in Figure 5(d). Then, we use the aligned ECG signals from the two experiments for BP estimation and compare their performance with the unaligned ECG signal (Figure 5(b)). The results on the PTT-PPG dataset show that the MAE for SBP estimation is improved from 3.28 to 2.95 in Experiment 1 and 2.87 in Experiment 2, respectively.

QRS Adaptive Search. The QRS complex represents rapid depolarization of the ventricular muscles of the heart [27, 36], a crucial phase in the cardiac cycle necessary for effective blood pumping. The configuration, duration, and orientation of the QRS complex provide vital insights into cardiac health and are pivotal in estimating blood pressure [14, 25]. SOTA models, e.g., RDDM [69], employ

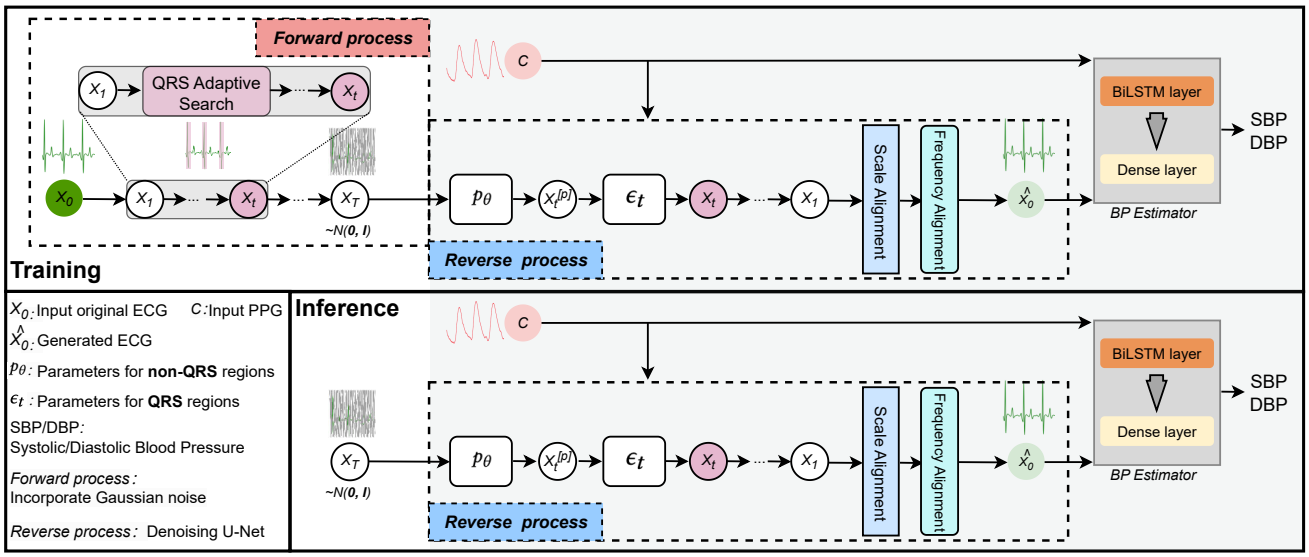

Figure 6: Overview of the proposed PPGG framework for blood pressure monitoring.

a fixed window approach to detect the QRS segment, which overlooks variations in the QRS complex that could indicate underlying cardiac conditions, such as changes in cardiac pumping capability, vascular resistance, or blood volume, which impact the efficiency of heart pumping. For instance, conditions like ventricular hypertrophy or intraventricular conduction delay can broaden the QRS complex [5, 6], potentially affecting cardiac output and thereby influencing blood pressure. Thus, we consider an adaptive approach for identifying the QRS segment, aiming to more accurately pinpoint its features and enable continuous and accurate tracking of BP changes.

3 PROPOSED MODEL

3.1 Overview

Inspired by our aforementioned motivations, we propose an end-to-end framework PPGG, as shown in Figure 6, which comprises a forward process incorporating a QRS adaptive search module and a reverse process that includes PPG-conditional denoising and scale-wise and frequency-wise alignment modules, finally followed by a blood pressure estimator. In the training phase, the pre-processed ECG is first fed into the forward process and then the PPG is injected into the reverse process as a condition, resulting in PPG-conditional generated ECG signals. Subsequently, both the PPG and the generated ECG are utilized for blood pressure estimation. In the inference phase, the model relies on only PPG input.

3.2 Forward Process

As shown in Figure 4, diffusion models [73] are composed of two phases. The forward process, denoted as $q(x_t|x_{t-1})$, operates with a Markov chain mechanism, systematically incorporating Gaussian noise at each sequential timestep, denoted by t.

$$q(x_T|x_0) = \prod_{t=1}^{T} q(x_t|x_{t-1}), \quad \text{where } q(x_t|x_{t-1}) \sim \mathcal{N}(x_t; \sqrt{1-\delta_t}x_{t-1}, \delta_t I). \tag{1}$$

Here, x_0 means a clean singal, and δ_t represents a small positive constant acquired from a fixed variance schedule $\delta_1, \delta_2, ..., \delta_T$. Define $\beta_t := 1 - \delta_t$ and $\overline{\beta_t} := \prod_{s=1}^{T} \beta_s$, then the forward process yields a sample at timestep t, notated as x_t:

$$x_t = \sqrt{\overline{\beta_t}}x_0 + \sqrt{1-\overline{\beta_t}}\epsilon, \quad \epsilon \sim \mathcal{N}(0, I). \tag{2}$$

We model the reverse process as a Markov chain by adopting a parameterized Gaussian transition $p_\theta(x_{t-1}|x_t)$.

$$p_\theta(x_{t-1}|x_t) \sim \mathcal{N}(x_{t-1}; \mu_0(x_t, t), \sigma_t^2 I), \tag{3}$$

where $\mu_0(x_t, t) = \frac{1}{\sqrt{\alpha_t}}\left(x_t - \frac{1-\beta_t}{\sqrt{1-\overline{\beta_t}}}\epsilon_t(x_t, t)\right)$. The diffusion model ϵ_t can be optimized based on the input signal c, making the conditional goal as:

$$L(\theta) = \|\epsilon - \epsilon_t(\sqrt{\overline{\beta_t}}x_0 + \sqrt{1-\overline{\beta_t}}\epsilon, c, t)\|^2. \tag{4}$$

In PPGG, we generate the ECG signals x_0 by using the corresponding PPG signal as the input condition c.

QRS adaptive search. Considering the crucial role of the QRS complex for BP monitoring, as shown in Figure 6, we incorporate a QRS adaptive search module into the standard forward process to adaptively locate specific regions of interest (ROI) (QRS or non-QRS) with the waveform's variation. The QRS region is dynamically selected as the region between the Q-peak and S-peak for each heartbeat.

Pan-Tompkins Algorithm [54] is used to detect R-peaks in the ECG signal in real time. The Pan-Tompkins algorithm is widely

applied in wearable devices and real-time monitoring systems [1, 35, 50] due to its simple structure, ease of implementation, and robust adaptability to various types of ECG signals. Specifically, the algorithm first applies a first-order derivative operator to compute the time derivative of the ECG signal. Then, the squared values of the derivative signal at each point are calculated. This step enhances the amplitude of the signal differences (especially at R-peaks), helping to further amplify the R-peak features. Next, a sliding window integration (or moving average) is applied to the squared signal, with the window size chosen to be approximately equivalent to the heart rate cycle. This integration smooths the signal and helps emphasize the QRS complex features.

Following this, a threshold based on the statistical data from previous heartbeats is dynamically adjusted to detect the R-peaks. Once the R-peak is detected, the Q-peak is typically identified as the first major wave before the R-peak by searching for a local minimum point before the R-peak. The S-peak occurs after the R-peak and is usually the first significant downward deflection. Similarly, the S-peak is detected by searching for a local minimum within a fixed window after the R-wave. Specifically, we use the first or second derivative of the ECG signal to locate the peaks and valleys, as the derivative tends to zero at these points. This approach ensures better accuracy in QRS complex detection, even under challenging conditions like signal noise or physiological variability. Consequently, we adopt a binary mask vector m with the same shape of x:

$$m[i] = \begin{cases} 1, & \text{if } i_q \le i \le i_s \\ 0, & \text{otherwise,} \end{cases} \tag{5}$$

where i_q indicates the QRS complex's Q-peak, located before the R-peak, and i_s refers to the S-peak, located after the R-peaks. After obtaining the mask vector m, we selectively and sequentially add noise to the QRS and non-QRS regions along the forward steps. Therefore, the QRS adaptive search-centric forward trajectory can be formulated as:

$$x_t = \sqrt{\overline{\beta_t}} x_0 + \sqrt{1 - \overline{\beta_t}}(m \cdot \epsilon), \quad \epsilon \sim \mathcal{N}(0, I). \tag{6}$$

where t is between 0 and T/2, followed by

$$x_t = \sqrt{\overline{\beta_t}} x_{T/2} + \sqrt{1 - \overline{\beta_t}}(\tilde{m} \cdot \epsilon), \quad \epsilon \sim \mathcal{N}(0, I). \tag{7}$$

where t is between T/2 and T, and $\tilde{m}$ means the mask vector for the non-QRS region, which is the bitwise NOT of m.

3.3 Reverse Process

In the reverse process, we estimate the reverse transition $p_\theta(x_t|x_T)$ by utilizing the objective L_q :

$$L_q = \lambda_1 \|(m \cdot \epsilon) - \epsilon_t(x_t, c, t)\|^2 + \lambda_2 \|(x_T - x_t) - \mathbf{x}_t^{[p]}\|^2, \tag{8}$$

where λ_1 and λ_2 are hyper-parameters. The first part learns to denoise the precise QRS complex, and the second part focuses on the non-QRS regions, clearly segregating the denoising process of critical ECG areas. λ_1 and λ_2 are set to 100 and 1, respectively, to emphasize the importance of denoising the QRS segment.

In detail, the L_q function guides the learning of ϵ_t for QRS refinement. Specifically, the first term $\|(m \cdot \epsilon) - \epsilon_t(x_t, c, t)\|^2$ enables ϵ_t to estimate noise which, once removed from the signal, improves the QRS morphology and detail fidelity. This is accomplished by reducing the difference between the QRS noise $(m \cdot \epsilon)$ and the noise generated by ϵ_t, which is responsible for learning and capturing both global and fine-grained details of the ECG signal, particularly those related to the critical QRS complexes that correspond to key cardiac electrical activity. In the second term, $\mathbf{x}_t^{[p]} = p_\theta(\mathbf{x}_t, c, t)$ learns to denoise the non-QRS parts of the ECG signals, thus $\|(x_T - x_t) - \mathbf{x}_t^{[p]}\|^2$ indicates the variance between non-QRS parts and the corresponding signal restored by $p_\theta(\mathbf{x}_t, c, t)$, ensuring the overall integrity of the ECG signals. The training algorithm of PPGG is outlined in Algorithm 1. The T is configured to a constant value of 50.

Algorithm 1 PPGG Training

repeat
- $\mathbf{x}_0 \sim q(\mathbf{x}_0)$
- $t \sim \text{Uniform}(\{1, \ldots, T\})$
- $\epsilon \sim \mathcal{N}(0, \mathbf{I})$
- Apply QRS mask: $m \cdot \epsilon$
- Compute $\mathbf{x}_T = \sqrt{\overline{\beta_t}} x_{T/2} + \sqrt{1 - \overline{\beta_t}}(\tilde{m} \cdot \epsilon)$
- Estimate $\mathbf{x}_t^{[p]} = p_\theta(\mathbf{x}_t, c, t)$
- Calculate $L_q = \lambda_1 \|(m \cdot \epsilon) - \epsilon_t(x_t, c, t)\|^2 + \lambda_2 \|(x_T - x_t) - \mathbf{x}_t^{[p]}\|^2$
- Calculate $L_a = L_{\text{scale}} + L_{\text{freq}}$
- Calculate $L_{\text{bp}} = \frac{1}{N} \sum_{i=1}^{N} \left(y_{\text{real},i} - y_{\text{pred},i}\right)^2$
- Calculate overall gradient as: $\nabla \left[L_q + L_a + L_{\text{bp}}\right]$

until converged

Alignment Modules. The correlation between ECG signals and blood pressure is mainly focused on the position of the R peak, the amplitude range, and the QRS complex. The QRS complex is aligned through the QRS adaptive search-guided forward process. To further improve the quality of the reconstructed ECG signals, we employ a scale alignment module and a frequency alignment module. In the former, the Pan-Tompkin [58] method is used to detect the R peaks in ECG. The loss for R-peak position alignment is given by the mean absolute error between the predicted R-peaks and the true R-peaks:

$$L_{\text{position}} = \frac{1}{N_{\min}} \sum_{i=1}^{N_{\min}} |p_{g_i} - p_{t_i}|, \tag{9}$$

where $N_{\min}$ is the minimum number of R-peaks between the generated and true ECG signals, p_{g_i} is the position of the i-th R-peak in the generated ECG, and p_{t_i} is the position of the i-th R-peak in the true ECG signal. For the amplitude alignment, we consider the maximum deviation in the amplitude within the signals:

$$L_{\text{amplitude}} = |E_g - E_t|, \tag{10}$$

where E_g represents the maximum amplitude difference of the generated ECG signal, and E_t represents the corresponding value in the true ECG signal. Therefore, the **scale alignment** loss can be calculated as:

$$L_{\text{scale}} = L_{\text{position}} + L_{\text{amplitude}}. \tag{11}$$

Similarly, in the **frequency alignment**, the loss function is denoted as L_{freq}, which is given by the absolute difference between the

generated and the target heart rate within a segment. Here, N_g represents the heart rate of the generated ECG, calculated as the number of corresponding R-peaks per unit time. N_t represents the corresponding part in the original ECG signal.

$$L_{\text{freq}} = |N_g - N_t|. \tag{12}$$

Finally, the loss function in alignment modules can be calculated as:

$$L_a = L_{\text{scale}} + L_{\text{freq}}. \tag{13}$$

3.4 Blood Pressure Estimator

For the blood pressure estimator, we opted for a Bidirectional Long Short-Term Memory (BiLSTM) model, which can create a comprehensive feature representation for the input signals [71]. And we show and explain the effects of different estimators in the subsequent Section 5.3. As shown in Figure 6, the generated ECG from the reverse process and the initial PPG signals are both fed into the BiLSTM layer, where the temporal features within the signals are captured. Specifically, BiLSTM connects the two hidden layers of LSTM to the output layer. Having two LSTMs as one layer enhances the learning of long-term dependencies and, along these lines, subsequently improves model performance. As the forward LSTM layer output sequence is obtained in a common way as the unidirectional one, the backward LSTM layer output sequence is calculated using the reversed inputs from time $t-1$ to $t-n$. These output sequences are then fed to be combined into an output vector $\mathbf{y_t}$. Similar to the LSTM layer, the final output of a BiLSTM layer can be represented by a vector, $\mathbf{Y_t} = [y_{t-n}, \ldots, y_{t-1}]$, in which the last element, y_{t-1}, is the estimated blood pressure for the next iteration. After feature extraction through the BiLSTM layer, the outputs are passed to a dense neural network layer. This layer has two neurons, each corresponding to a blood pressure type: one for SBP and the other for DBP. This layer's function is essentially a regression task where the learned features from the BiLSTM are mapped to blood pressure values. The weights in this dense layer learn to predict blood pressure based on the temporal features provided by the BiLSTM. The loss function for BP estimation is: $L_{\text{bp}} = \frac{1}{N}\sum_{i=1}^{N}\left(y_{\text{real},i} - y_{\text{pred},i}\right)^2$, where y_{real} and y_{pred} represent the real and predicted values of BP, respectively.

Overall training objective. In our proposed PPGG, the overall training objective is summarized as follows:

$$\mathcal{L}_{\text{overall}} = L_q + L_a + L_{\text{bp}} \tag{14}$$

4 EXPERIMENTS

4.1 Datasets and Implementation Details

Datasets. Our experiments are mainly conducted based on two public datasets and a self-collected dataset. The **PTT-PPG** dataset, released in 2022 [45], contains data collected from 22 healthy subjects at the University of Sydney as they engaged in three activities. It includes PPG signals, inertial data, ECG signals, blood pressure, and SpO2 levels. The activities performed in random order were sitting, stationary, walking, and running. The **MIMIC II** dataset [62] was compiled by MIT researchers. It contains anonymized records of ICU patients. It consists of thousands of PPG, ECG, and BP signals recorded from various hospitals between 2001 and 2008.

Table 1: Statistics of MIMIC II and PTT-PPG Datasets.

	MIMIC II	PTT-PPG
Age range	15∼101	20∼53
Average age	65.5	28.5
Female (%)	9,013 (43.8%)	6 (27.3%)
Male (%)	17,857 (56.2%)	16 (72.7%)
Subjects	26,870	22
Data source	Patients with bedside monitors	healthy subjects at USYD
Sampling rate (Hz)	125	500
PPG device	Philips IntelliVue / GE Healthcare Bedside Monitors	MAX30101 PPG sensors
ECG device	Philips IntelliVue / GE Healthcare Bedside Monitors	Not mentioned

The BP data come from various sources: AOBP (Automated Office Blood Pressure), NBP (Noninvasive Arterial Blood Pressure), and PAWP (Pulmonary Artery Wedge Pressure). These measurement methods provide us with blood pressure readings under different conditions, aiding in the assessment and monitoring of cardiovascular health. **Our self-collected dataset** was conducted by two individuals (one female and one male), measuring blood pressure changes before and after meals, reflecting the physiological effects of digestion. We use an Omron cuff BP monitor for measuring blood pressure, a Polar device for sensing ECG, and a Mi4 Smart Band for collecting PPG. The blood pressure was measured every 10 minutes before and after meals while ECG and PPG data were continuously recorded. We focused on the half-hour intervals around meal times to evaluate the sensitivity and accuracy of detecting blood pressure fluctuations due to dietary intake.

Dataset analysis. Table 1 highlights the key differences between the MIMIC II and PTT-PPG datasets. The MIMIC II dataset has a broad age range from 15 to 101 years, with an average age of 65.5 years. It includes 9,013 females (43.8%) and 17,857 males (56.2%). High-end devices such as the Philips IntelliVue [57] and GE Healthcare Bedside Monitors [22] were used to collect PPG and ECG data, with a sampling frequency of 125 Hz. Additionally, MIMIC II includes detailed patient data collected in intensive care units, such as vital signs, medications, laboratory results, and more, offering a comprehensive view of patient care and outcomes. In contrast, the PTT-PPG dataset is more narrowly focused, with an age range of 20 to 53 years and an average age of 28.5 years. It includes 6 females (27.3%) and 16 males (72.7%). Data collection for PTT-PPG comes from the University of Sydney and includes devices such as the MAX30101 PPG sensors. The sampling frequency for PPG and ECG data in this dataset is 500Hz. The smaller, more homogeneous sample size of PTT-PPG makes it more suited for specific, controlled studies rather than broad clinical applications. Overall, MIMIC II offers a more diverse and extensive dataset derived from clinical settings, and PTT-PPG provides a focused dataset with specific age and gender distributions.

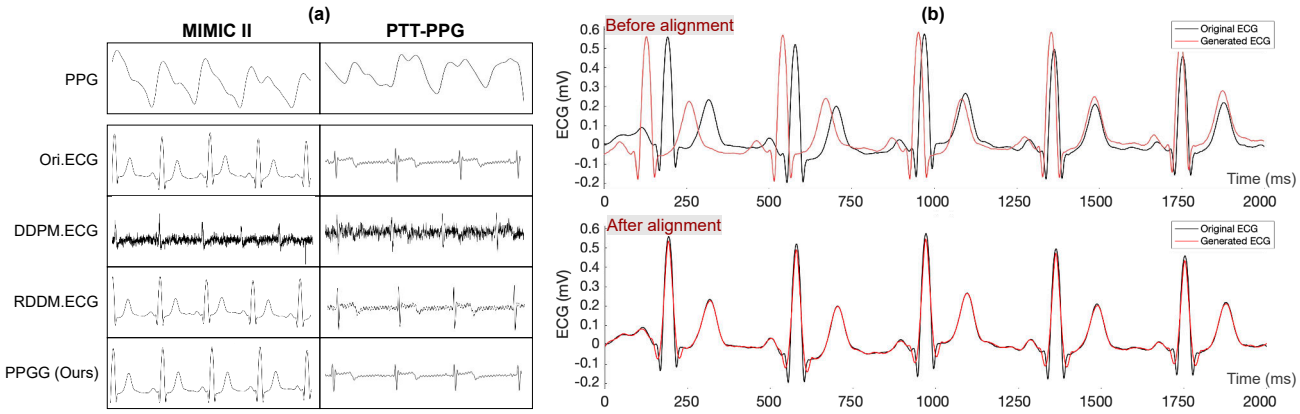

Figure 7: (a) Visual comparison of reconstructed ECG signals on the MIMIC II and PTT-PPG datasets. The left-side coordinates represent the original PPG, the original ECG, and the reconstructed ECG generated by DDPM, RDDM, and PPGG. PPGG consistently outperforms DDPM and RDDM. (b) Visual comparison of reconstructed ECG and original ECG with and without two alignments on the MIMIC II dataset.

Data pre-processing. Our approach adheres to established protocols [43] for ECG and PPG signals. Initially, we conduct a resampling of both modalities to a frequency of 125 Hz. This is followed by a highpass filter of the Butterworth variety, with a threshold frequency of 0.5 Hz, to the ECG data. In parallel, PPG data undergo a filtration process utilizing a Butterworth filter that operates within a bandpass range of 0.5 to 8 Hz. To account for inter-subject variability, we implement z-score normalization on a per-subject basis. The final step involves the segmentation of the signals into windows of 4 seconds each, serving as the foundational data for training our model. Each dataset is randomly split into a training set (80%) and a test set (20%).

Train setup. PPGG is optimized on 2 NVIDIA A100 GPUs, utilizing a batch size of 512. The optimization process is governed by the AdamW algorithm. This configuration is sustained throughout 400 epochs. We implement a consistent linear variance scheduler, with the β parameter ranging from 0.0001 to 0.2, details of which are elaborated in Section 5.

Models in comparison. We compare PPGG with various generative models. **CycleGAN** [44] uses a cycle generative adversarial network which extends the GAN architecture to generate ECG from PPG for blood pressure estimation. **GDCAE** [61] is an autoencoder-based generative model for BP estimation using PPG with the assumption that PPG signals strongly correlate with arterial blood pressure. **DDPM** [29] is a generative model that mimics the physical process of diffusion to create complex data distributions. It operates on the principle of gradually removing noise from a completely random distribution to generate structured data resembling the target output when applied to blood pressure estimation tasks. **RDDM** [69] is a new diffusion model developed to represent the complex temporal dynamics of ECG signals.

4.2 Evaluation Metrics

We evaluate model performance using two metrics: Mean Absolute Error (MAE) and Root Mean Square Error (RMSE). The results will be calculated separately for SBP and DBP. The corresponding formulas are as follows: MAE $= \frac{1}{N}\sum_{i=1}^{N}|y_i - \hat{y}_i|$, where y_i is the true BP value, $\hat{y}_i$ is the predicted BP value, and N is the number of observations. Since MAE calculates the average of the absolute differences between the predicted and actual BP values, it directly reflects the average deviation, providing an overall error level of the PPGG model in BP estimation. RMSE $= \sqrt{\frac{1}{N}\sum_{i=1}^{N}(y_i - \hat{y}_i)^2}$, where y_i, $\hat{y}_i$, and N are defined as above. RMSE is the square root of the mean of the squared errors, better capturing the impact of larger errors. The squaring operation amplifies larger errors, making RMSE more sensitive to them than MAE. RMSE offers a better assessment of the PPGG model's performance in predicting extreme values.

5 RESULTS

5.1 Visualization

Figure 7(a) visualizes an example segment of PPG signals (PPGs) and ECG signals (ECGs) from the two datasets, as well as the ECGs generated from PPGs by different models, including DDPM, RDDM and PPGG. The ECGs generated by PPGG exhibit remarkably high fidelity compared to the original ECG. ECGs generated by DDPM deviate significantly from the original signals and exhibit greater noise, failing to replicate the complex structure and frequency of QRS waves. Additionally, while RDDM preserves much of the QRS wave signal, there are still phenomena such as misaligned R-peaks (especially in MIMIC II) and significant differences in amplitudes. In stark contrast, PPGG maintains high fidelity in both the temporal and frequency domains, accurately restoring signal characteristics. Figure 7(b) compares the results with and without two alignment modules. Both the scale-wise and frequency-wise alignment modules contribute to highly faithful peak restoration and refinement of signal details.

Table 2: Comparison of various generative models.

Dataset	PTT-PPG				MIMIC II			
Method	**$RMSE_{SBP}$**	**$RMSE_{DBP}$**	**MAE_{SBP}**	**MAE_{DBP}**	**$RMSE_{SBP}$**	**$RMSE_{DBP}$**	**MAE_{SBP}**	**MAE_{DBP}**
CycleGAN [44]	10.42	8.26	8.15	4.87	8.78	5.48	6.32	3.89
GDCAE [61]	8.57	5.10	5.88	3.03	5.19	2.76	3.81	2.00
DDPM [29]	6.63	3.94	5.27	2.45	6.03	3.21	4.26	1.35
RDDM [69]	4.82	3.06	3.28	2.19	4.94	2.88	3.57	2.14
PPGG(Ours)	**3.22**	**2.49**	**2.16**	**1.85**	**2.92**	**1.40**	**2.18**	**1.27**

Table 3: Comparison of different end-to-end methods.

Method	Test modality	MAE_{SBP}	MAE_{DBP}
CNN [7]	PPG & ECG	11.17	5.35
MLR [17]	PPG & ECG	5.28	3.95
U-Net [42]	PPG & ECG	**2.12**	1.79
SVM [33]	PPG	11.64	7.62
NN [41]	PPG	13.40	6.98
U-Net [42]	PPG	8.39	5.87
LSTM [48]	PPG	8.92	6.14
BiLSTM [39]	PPG	7.85	4.42
PPGG (Ours)	PPG	2.18	**1.27**

Table 4: Comparing different blood pressure estimators.

Test modality	Estimator	MAE_{SBP}	MAE_{DBP}
Ori.PPG	U-Net	3.78	2.40
Ori.PPG + Gen.ECG	U-Net	2.94	1.61
Ori.PPG + Gen.ECG	LSTM	3.26	2.05
Ori.PPG + Gen.ECG	BiLSTM	**2.18**	**1.27**

Table 5: Results of ablation study in the PTT-PPG dataset (SA: scale alignment, FA: frequency alignment).

Method	$RMSE_{SBP}$	$RMSE_{DBP}$	MAE_{SBP}	MAE_{DBP}
w/o SA	4.15	3.17	3.03	2.18
w/o FA	3.48	2.62	2.38	1.96
w/o SA&FA	4.79	3.39	3.16	2.32
PPGG	**3.22**	**2.49**	**2.16**	**1.85**

5.2 Overall Performance

As shown in Table 2, PPGG maintains its superiority across different top-performing generative methods. On the PTT-PPG dataset, it achieves MAE_{SBP} of 2.16 and MAE_{DBP} of 1.85, along with $RMSE_{SBP}$ of 3.22 and $RMSE_{DBP}$ of 2.49. On the MIMIC II dataset, the higher quality of the original signals leads to more accurate blood pressure prediction, with an impressive RMSE of 1.40 for DBP, surpassing other comparative models significantly. These observations indicate that PPGG captures finer-grained signal features in ECG generation.

Table 3 illustrates the performance comparison of different end-to-end models for BP estimation with the MIMIC II dataset. Among the models tested solely with PPG, such as CNN, SVM, and NN, PPGG demonstrates significant superiority, with an MAE_{SBP} of 2.18, far surpassing similar models. In models tested with both PPG and ECG, PPGG maintains its advantage by utilizing PPG and the corresponding generated ECG, outperforming most models such as MLR [17] and CNN [7]. Although its MAE_{SBP} result slightly trails U-Net, the difference is marginal, and PPGG possesses the inherent advantage of requiring only PPG as input.

5.3 Comparing Different Blood Pressure Estimators

In the blood pressure estimation section, we experiment with several different models, including U-Net, LSTM, and BiLSTM. The results are presented in Table 4. The best-performing estimator is BiLSTM. The average MAE for estimating SBP and DBP are 2.18 and 1.27 respectively. The reason behind is that blood pressure is influenced by patterns within both past and future ECG signal segments. Therefore, the BiLSTM-based BP estimator, which processes information in both forward and backward directions, are well-suited for understanding these relationships, leading to more precise estimations. In addition, the BiLSTM model excels at learning long-term dependencies, which is crucial for physiological signals like ECG and blood pressure that have long-range correlations. Other models, such as traditional LSTM or simple feedforward networks, can not capture such dependencies as effectively.

5.4 Ablation Study

This section presents the effectiveness of the QRS adaptive search module, the scale alignment module, and the frequency alignment module.

QRS adaptive search. To evaluate the effectiveness of the QRS adaptive search module, we replace the ROI window used in RDDM [69], which is fixed at 32, with the QRS adaptive search proposed in this paper. By doing so, the average $RMSE_{SBP}$ decreases from 4.94 to 4.68, and the average $RMSE_{DBP}$ decreases from 2.88 to 2.73 in the MIMIC II dataset. This demonstrates that the QRS wave, being the most prominent wave in the ECG and closely related to heart contractions, adapts better to heart activity changes when dynamically searching for the QRS range compared to a fixed window.

Scale alignment. This module is employed to ensure the high-fidelity reconstruction of ECG signals, preserving both the position of the R-peaks and the overall signal range of the original ECG. As outlined in Table 5, upon removing the scale alignment module, all metrics exhibit a noticeable deterioration, e.g., the average $RMSE_{SBP}$ increasing from 3.22 to 4.15 and the average MAE_{SBP} increasing

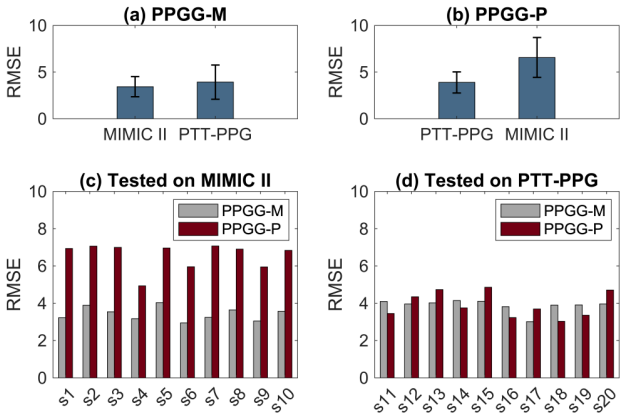

Figure 8: Results of cross-dataset validation.

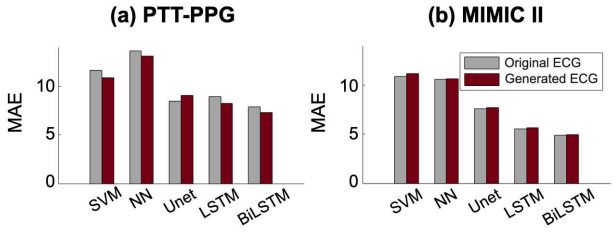

Figure 9: Comparing the effectiveness of the generated ECG and original ECG.

from 2.16 to 3.03. This underscores the crucial role of the scale-wise alignment module in the reconstruction process.

Frequency alignment. Similarly, in data with higher levels of noise, the frequency alignment module also plays a role. Upon its removal, the average RMSE_{SBP} increases by 0.26. This is because the frequency of R-peaks is crucial in noisy environments, serving as a key discriminator between noise and the original signal. For example, when there is significant noise interference, within the same time window, the number of R-peaks in the original ECG signal and the generated ECG signal may differ. L_{position} only ensures that the first N_{min} R-peaks remain aligned, while L_{freq} further constrains the number of generated R-peaks.

5.5 Cross-dataset Validation

Cross-dataset evaluation serves to assess the generalizability and efficacy of models across diverse data sources. The purpose of this experiment is to ensure that the model does not excessively adapt to the idiosyncrasies and particular characteristics of the training dataset. In this experiment, we train PPGG using the MIMIC II and PTT-PPG datasets, respectively, and compare their performances using the other dataset. In the following, for simplicity, we refer to the PPGG model trained by the MIMIC II dataset as **PPGG-M**, and the one trained by the PTT-PPG dataset as **PPGG-P**. We extract 100 untrained data samples from MIMIC II and randomly divide them into 10 equal validation submissions, i.e., $s1$ to $s10$. Similarly, another 100 untrained data samples are extracted from PTT-PPG, and divided into 10 validation submissions, i.e., $s11$ to $s20$. PPGG-M and PPGG-P are validated with all the 20 submissions.

Figure 8 depicts the RMSE of the SBP estimation in the cross-dataset validation experiments. Fig. 8(a) shows the performance of PPGG-M on the MIMIC II and PTT-PPG datasets. Its average RMSE_{SBP} on MIMIC II (the training dataset) is 3.43, and slightly increases to 3.92 when the model is tested with the unseen PTT-PPG dataset. Fig. 8(b) presents the performance of PPGG-P on the test datasets. The average RMSE_{SBP} on PTT-PPG (the training dataset) is 3.89, and increases to 6.56 when validated with the unseen MIMIC II dataset. We further look into the experiment details by examining the results from each of the validation submissions. Fig. 8(c) compares the performance differences of PPGG-M and PPGG-P on $s1$ to $s10$ (from MIMIC II dataset). It can be observed that PPGG-P cannot sustain good performance when tested on the MIMIC II dataset, and the RMSE_{SBP} is much higher than that of PPGG-M in all the validation experiments with $s1$~$s10$. Fig. 8(d) presents the performance of PPGG-M and PPGG-P on $s11$ to $s20$ (from PTT-PPG dataset). Different from PPGG-P on the MIMIC II dataset, PPGG-M can achieve comparable performance with PPGG-P when tested on the PTT-PPG dataset, their RMSE_{SBP} keeps similar across all the validations with $s11$~$s20$.

The performance differences of PPGG-M and PPGG-P are probably due to the different qualities of the two datasets. If trained with a comprehensive dataset, like MIMIC II, PPGG exhibits promising generalizability and transferability. While training with a limited dataset like PTT-PPG can easily result in an over-fitted and unreliable model.

5.6 Generated ECG v.s. Original ECG

We evaluate the quality of the ECG signals generated by PPGG using a comparative experiment. The PPGG model used in this experiment is trained by the MIMIC II dataset, and uses the PPG signals in the test data (not used in the training phase) from the two public datasets as inputs to generate ECG signals, and then compares the quality of the generated ECG with the original ECG in the test data.

We adopt several popular models from the literature to estimate SBP using the generated ECG and the original ECG as inputs, respectively, and then compare their performance. Figure 9 compares the MAE of the estimated SBP with five different models, including SVM, NN, U-net, LSTM, and BiLSTM. The grey bar represents the estimated results from the original ECG, while the dark red bar represents the results from the generated ECG. Although the performance of different models varies, it is evident that whether using generated ECG or the original ECG signals, all models yield consistent results when we compare the two signals. Among the tested models, the best SBP estimation performance is achieved by BiLSTM in both datasets. In the MIMIC II dataset, as shown in Fig. 9(b), the generated ECG closely approximates the performance of the original ECG. In the PTT-PPG dataset, as reported in Fig. 9(a), the generated ECG surprisingly outperforms the original ECG in most models, including SVM, U-net, LSTM, and BiLSTM. The experiment results demonstrate PPGG's powerful ability to generate high-quality ECG signals for BP estimation with PPG signals as inputs. In noisy datasets, like PTT-PPG, the generated ECG actually achieves even better results than the original ECG.

Table 6: Comparing blood pressure estimation using different region-of-interest (QRS v.s. P-QRS-T).

Submission	s1	s2	s3	s4
QRS ($RMSE_{SBP}$)	3.48	3.29	3.37	3.35
P-QRS-T ($RMSE_{SBP}$)	3.11	2.95	3.26	3.20

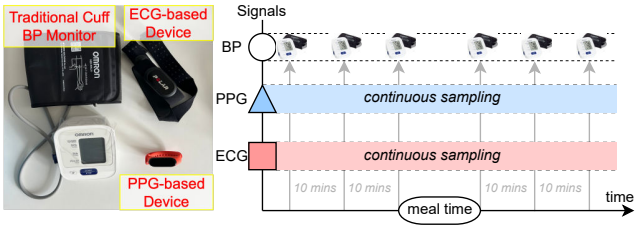

Figure 10: Experiment setup in our case study.

This implies that by utilizing the low-cost and convenient PPG signals, PPGG can generate near-perfect ECGs for BP estimation tasks, thereby achieving both high convenience and optimal accuracy in BP monitoring.

5.7 More on QRS Adaptive Search

As discussed in Section 2, in addition to the QRS waveform, the P wave and T wave in ECG are also intrinsically linked to blood pressure. To verify the potential of adding the P wave and T wave to the region of interest (ROI) in the forward process, we extend the QRS adaptive search, by incorporating the P wave and T wave, into the P-QRS-T adaptive search. Specifically, we selected 200 sequences that have distinct P waves and T waves on the MIMIC II dataset for training and an additional 4 sequences for validation. Table 6 shows the results when we expand the ROI to include the complete P-QRS-T waveform (while differentiating between all waveforms) compared to selecting only the QRS segment. We see that the complete P-QRS-T waveform is clearly more beneficial for blood pressure prediction.

However, it is worth noting that these sequences, where the complete P-QRS-T waveform in ECGs can be distinctly identified, only constitute 1.53% of the 13,312 sequences in the MIMIC II training dataset. Training models solely on these few high-quality sequences greatly increases the likelihood of model overfitting, preventing the model from learning the broad features of the data, which results in low monitoring accuracy in practical applications. In reality, the challenges of distinguishing between P waves and T waves in ECG signals arise from various factors, including signal noise caused by the environment and equipment, the relatively small amplitude of the ECG signal itself, waveform overlap during tachycardia, limitations of ECG acquisition techniques, lack of experience in interpretation by operators, and physiological differences in the human body. These issues can lead to unclear or ambiguous waveform characteristics in the ECG, affecting diagnostic accuracy, which calls for future research efforts.

Table 7: MAE for the female participant over 3 days.

	Day1		Day2		Day3	
	SBP	DBP	SBP	DBP	SBP	DBP
MAE	4.93	3.86	4.98	3.83	4.87	3.85

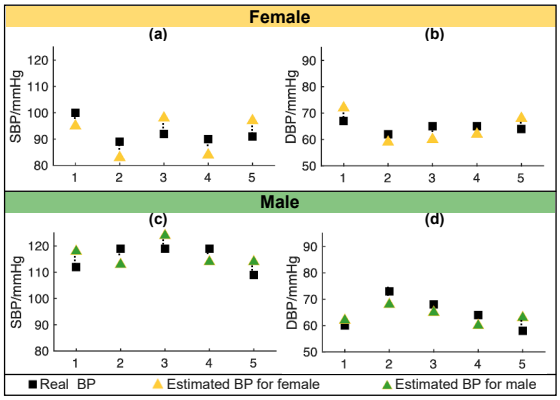

Figure 11: The comparison of real and estimated blood pressure throughout one day.

5.8 Real-world Case Study

To evaluate the continuous performance of PPGG in a practical scenario, we conduct a case study in real-world environments. The blood pressure of healthy individuals typically undergoes changes within 30 minutes postprandially and gradually returns to baseline levels. This is due to the activation of the digestive system and the redistribution of blood to the gastrointestinal tract, resulting in temporary blood pressure fluctuations. Therefore, we utilize a half-hour interval before and after meals to investigate the sensitivity and accuracy of PPGG in detecting blood pressure variations during common daily eating activities. The experiment setup involves three devices: a traditional cuff BP monitor (Omron) for measuring blood pressure, a Polar device for collecting ECG signals, and a Mi4 Smart Band device for collecting PPG data, as shown in Figure 10. The experiment procedure is as follows. The collection of ECG and PPG data spans the entire duration of the experiment. Blood pressure is measured at 10-minute intervals before and after the meal. We recruited two volunteers, a 29-year-old male and a 26-year-old female. The two participants conducted data collection according to the aforementioned protocol. The man collected data for a single day, while the woman collected data over three consecutive days, focusing on lunch each day. The design of this case study is intended merely to test the feasibility of continuous monitoring using the model in real-world scenarios. As we have conducted extensive experimental evaluation of our model on the two public datasets, we believe the participation of two subjects is sufficient for this purpose.

In this experiment, we train PPGG using both datasets and fine-tune the model using only 5% of the collected PPG and ECG data to better adapt to the characteristics and distribution of the new dataset. Table 7 displays the daily measurement accuracy for the female tester. The MAE of SBP initially increases and then decreases on the 3rd day, while DBP consistently decreases over time. Overall,

both SBP and DBP demonstrate that as time progresses, the accuracy of the model improves. Figure 11 presents the detailed real and estimated BP measurements for the 2 participants throughout one day. The black square represents the real SBP and DBP value collected by the cuff BP monitor and the triangles represent the estimated BP using PPGG. Figure 11(a) and (b) show the estimated BP for the female, with the MAE of SBP and DBP being 4.93 and 3.86, respectively. Figure 11(c) and (d) display the estimated blood pressure for the male, with the MAE of SBP and DBP being 4.91 and 3.83, respectively. Notably, in the male DBP comparison, we can see that the estimated values more closely approximate the real BP values. Overall, the MAE for both SBP and DBP of the male is lower than that of the female. The performance of PPGG in this real-world case study meets the standards for non-invasive sphygmomanometers like the ISO 81060-2 standard [56] and the British standard [11].

5.9 Model Size and Overhead

The PPGG model, with a size of 725.3MB and an inference memory usage of approximately 1,442MB, contains a total of 168,245,600 parameters. The average inference time per instance is 304 ms, derived from 500 inferences on a MacBook Pro 2023 laptop equipped with an Apple M2 Pro chip and 16 GB of memory. To evaluate the on-device performance of our model on mobile platforms, we also tested it using the Samsung S23 Ultra mobile phone, which is quipped with a Qualcomm Snapdragon 8 Gen 2 processor, 8 GB of RAM, 256 GB of storage and a 5000 mAh battery, running Android 13. The average inference time per instance is 1.45 seconds based on 200 iterations. This opens up the possibility for real-time blood pressure estimation and ECG generation directly on mobile platforms, significantly enhancing accessibility for practical use. In the future, we plan to further optimize the model for more efficient deployment on mobile devices and use embedded sensors [82, 83, 85, 86] to enhance the framework.

6 RELATED WORK

Blood Pressure Measurement. Blood pressure (BP) was initially estimated indirectly through biomechanical and mathematical modeling. FK Forster *et al.* [19] introduced a theoretical model for oscillometric BP measurement, indicating that mean BP can be predicted from the oscillometric curve's peak with adjustments for cuff pressure waveform. Similarly, Ursino *et al.* [77] investigated a mathematical model on the biomechanics of arterial walls under external pressure, showing how tissue mechanics and blood flow dynamics can impact BP measurements. Contrarily, KJ Kim *et al.* [34] found that although the cuff pressure significantly deforms the arm tissue, it does not similarly affect the artery wall. These models often simplify the cardiovascular system and overlook individual variations, which leads to inaccuracies in BP estimation.

In addition to the PPG and ECG, several other features have been utilized for estimating BP, such as Pulse Transit Time (PTT) [20, 23, 55, 70], Pulse Wave Velocity (PWV) [26, 53, 74], and Ballistocardiography (BCG) [12, 47, 68]. However, PTT is highly sensitive to non-blood pressure factors and varies significantly among individuals. PWV is strongly dependent on arterial elasticity, suggesting that it can be influenced by factors like age, potentially skewing BP estimates. Moreover, the accuracy of BCG is closely linked to the quality of the measuring equipment and is susceptible to distortions caused by physical movements, leading to inaccurate BP assessments. Over the years, BP estimation has also evolved from relying on a single model or modality to utilizing multiple ones. Jain *et al.* [32] developed a system that employs various signals (ECG and PPG) to gauge BP. Ye *et al.* [84] introduced a multi-model integration of classifiers for predicting BP levels. Nevertheless, these methods still fall short in providing long-term, continuous, and convenient BP monitoring.

PPG-to-ECG Conversion. PPG-to-ECG conversion works can be divided into three categories: Bio-feature-based, CNN-based, and generative model-based. Firstly, Banerjee *et al.* [8] and Tian *et al.* [75] both focused on developing computational parametric models to extract specific cardiac features from PPG signals for ECG reconstruction. However, they failed to capture the nonlinear relationship between the two domains. This issue was later investigated through CNN-based models. Reiss *et al.* [59] discussed a large-scale application of CNN for heart rate estimation from PPG, which is relevant for ECG reconstruction. To incorporate temporal information, Chiu *et al.* [13] presented a transformed attentional convolutional network model for converting PPG signals to ECG signals. However, these methods do not consider the specific requirements for blood pressure estimation, making them difficult to apply to tasks requiring accurate BP estimation. CardioGAN [65] was the first attempt to use generative models for direct PPG to ECG conversion based on CycleGAN [13]. Empirically, they demonstrated that the HR estimation from the generated ECG was significantly better compared to the original PPG. Golany *et al.* [24] and Adib *et al.* [3] generate ECGs from input noise to augment the available ECG training set to enhance arrhythmia detection. RDDM [69] is a diffusion model for cross-modal biosignal conversion. These methods struggle with preserving critical details such as the R-peaks, signal range, and QRS complex. These deficiencies impair the model's effectiveness in consistently and accurately monitoring BP situations that require precise ECG signal interpretation. As a result, they fail to effectively manage the substantial entropy reduction during the generation process, resulting in unsatisfactory performance in estimating the blood pressure.

7 CONCLUSION

This paper proposes the first end-to-end diffusion model based framework PPGG, which generates high-fidelity ECG signals with PPG condition, for predicting blood pressure. PPGG incorporates the QRS adaptive search module in the forward process and the scale alignment and frequency alignment modules in the reverse process, and achieves ECG-level performance for blood pressure monitoring using only the low-cost and convenient PPG signal. Extensive experimental evaluations on three datasets demonstrate the superior performance of PPGG for blood pressure monitoring and indicate PPGG's ability to offer an effective solution for long-term, continuous, and low-cost blood pressure monitoring. In the future, we plan to further optimize the model for efficient deployment on mobile devices.

REFERENCES

[1] U Rajendra Acharya, Hamido Fujita, Shu Lih Oh, Yuki Hagiwara, Jen Hong Tan, and Muhammad Adam. 2017. Application of deep convolutional neural network for automated detection of myocardial infarction using ECG signals. *Information Sciences* 415 (2017), 190–198.

[2] Juul Achten and Asker E Jeukendrup. 2003. Heart rate monitoring: applications and limitations. *Sports medicine* 33 (2003), 517–538.

[3] Edmonmd Adib, Amanda S Fernandez, Fatemeh Afghah, and John J Prevost. 2023. Synthetic ECG signal generation using probabilistic diffusion models. *IEEE Access* 11 (2023), 75818–75828.

[4] Robert Avram, Jeffrey E Olgin, Peter Kuhar, J Weston Hughes, Gregory M Marcus, Mark J Pletcher, Kirstin Aschbacher, and Geoffrey H Tison. 2020. A digital biomarker of diabetes from smartphone-based vascular signals. *Nature medicine* 26, 10 (2020), 1576–1582.

[5] Ljuba Bacharova. 2019. Missing link between molecular aspects of ventricular arrhythmias and QRS complex morphology in left ventricular hypertrophy. *International Journal of Molecular Sciences* 21, 1 (2019), 48.

[6] Ljuba Bacharova, Vavrinec Szathmary, Matej Kovalcik, and Anton Mateasik. 2010. Effect of changes in left ventricular anatomy and conduction velocity on the QRS voltage and morphology in left ventricular hypertrophy: a model study. *Journal of electrocardiology* 43, 3 (2010), 200–208.

[7] Sanghyun Baek, Jiyong Jang, and Sungroh Yoon. 2019. End-to-end blood pressure prediction via fully convolutional networks. *Ieee Access* 7 (2019), 185458–185468.

[8] Rohan Banerjee, Aniruddha Sinha, Anirban Dutta Choudhury, and Aishwarya Visvanathan. 2014. PhotoECG: Photoplethysmographyto estimate ECG parameters. In *2014 IEEE International Conference on Acoustics, Speech and Signal Processing (ICASSP)*. IEEE, 4404–4408.

[9] Amir Benmira, Antonia Perez-Martin, Iris Schuster, Isabelle Aichoun, S Coudray, F Bereksi-Reguig, and M Dauzat. 2016. From Korotkoff and Marey to automatic non-invasive oscillometric blood pressure measurement: does easiness come with reliability? *Expert review of medical devices* 13, 2 (2016), 179–189.

[10] Jeremy Booth. 1977. A short history of blood pressure measurement. *Proceedings of the Royal Society of Medicine* 70 (1977), 793–799.

[11] British Standards Institution. 2004. Non-invasive sphygmomanometers - Part 4: Automated measurement type. BS EN 1060-4:2004.

[12] R. Casanella, J. Gomez-Clapers, and R. Pallas-Areny. 2012. On time interval measurements using BCG. In *2012 Annual International Conference of the IEEE Engineering in Medicine and Biology Society*. 5034–5037.

[13] Hong-Yu Chiu, Hong-Han Shuai, and Paul C-P Chao. 2020. Reconstructing QRS complex from PPG by transformed attentional neural networks. *IEEE Sensors Journal* 20, 20 (2020), 12374–12383.

[14] Mary Boudreau Conover. 2002. *Understanding electrocardiography*. Elsevier Health Sciences.

[15] Steven Daniels, Abdulmassih S Iskandrian, A-Hamid Hakki, Sally A Kane, Charles E Bemis, Leonard N Horowitz, Allan M Greenspan, and Bernard L Segal. 1984. Correlation between changes in R wave amplitude and left ventricular volume induced by rapid atrial pacing. *American Heart Journal* 107, 4 (1984), 711–717.

[16] Chadi El-Hajj and Panayiotis A Kyriacou. 2020. A review of machine learning techniques in photoplethysmography for the non-invasive cuff-less measurement of blood pressure. *Biomedical Signal Processing and Control* 58 (2020), 101870.

[17] Heesang Eom, Dongseok Lee, Seungwoo Han, Yuli Sun Hariyani, Yonggyu Lim, Illsoo Sohn, Kwangsuk Park, and Cheolsoo Park. 2020. End-to-end deep learning architecture for continuous blood pressure estimation using attention mechanism. *Sensors* 20, 8 (2020), 2338.

[18] Marc Feissel, Frédéric Michard, Isabelle Mangin, Olivier Ruyer, Jean-Pierre Faller, and Jean-Louis Teboul. 2001. Respiratory changes in aortic blood velocity as an indicator of fluid responsiveness in ventilated patients with septic shock. *Chest* 119, 3 (2001), 867–873.

[19] F K_ Forster and D Turney. 1986. Oscillometric determination of diastolic, mean and systolic blood pressure—a numerical model. *Journal of biomechanical engineering* 108 (1986), 359–364.

[20] Mingwu Gao, N Bari Olivier, and Ramakrishna Mukkamala. 2016. Comparison of noninvasive pulse transit time estimates as markers of blood pressure using invasive pulse transit time measurements as a reference. *Physiological reports* 4, 10 (2016), e12768.

[21] Aman Gaurav, Maram Maheedhar, Vijay N Tiwari, and Rangavittal Narayanan. 2016. Cuff-less PPG based continuous blood pressure monitoring—A smartphone based approach. In *2016 38th annual international conference of the IEEE engineering in medicine and biology society*. IEEE, 607–610.

[22] GE Healthcare. 2023. Patient Monitoring Solutions. https://www.gehealthcare.com/products/patient-monitoring. Accessed: 2024-06-25.

[23] Heiko Gesche, Detlef Grosskurth, Gert Küchler, and Andreas Patzak. 2012. Continuous blood pressure measurement by using the pulse transit time: comparison to a cuff-based method. *European journal of applied physiology* 112, 1 (2012), 309–315.

[24] Tomer Golany, Gal Lavee, Shai Tejman Yarden, and Kira Radinsky. 2020. Improving ECG classification using generative adversarial networks. In *Proceedings of the AAAI conference on artificial intelligence*, Vol. 34. 13280–13285.

[25] Ary L Goldberger, Zachary D Goldberger, and Alexei Shvilkin. 2017. *Clinical Electrocardiography: A Simplified Approach: Clinical Electrocardiography: A Simplified Approach E-Book*. Elsevier Health Sciences.

[26] Sara V Greve, Stephan Laurent, and Michael H Olsen. 2017. Estimated pulse wave velocity calculated from age and mean arterial blood pressure. *Pulse* 4, 4 (2017), 175–179.

[27] John Hampton and Joanna Hampton. 2019. *The ECG Made Easy E-Book: The ECG Made Easy E-Book*. Elsevier Health Sciences.

[28] Awni Y Hannun, Pranav Rajpurkar, Masoumeh Haghpanahi, Geoffrey H Tison, Codie Bourn, Mintu P Turakhia, and Andrew Y Ng. 2019. Cardiologist-level arrhythmia detection and classification in ambulatory electrocardiograms using a deep neural network. *Nature medicine* 25, 1 (2019), 65–69.

[29] Jonathan Ho, Ajay Jain, and Pieter Abbeel. 2020. Denoising diffusion probabilistic models. *Advances in neural information processing systems* 33 (2020), 6840–6851.

[30] Tobore Igbe, Jingzhen Li, Yuhang Liu, Sinan Li, Abhishek Kandwal, Zedong Nie, and Wang Lei. 2019. Analysis of ECG segments for non-invasive blood glucose monitoring. In *2019 IEEE International Conference on E-health Networking, Application & Services*. IEEE, 1–6.

[31] Siti Nor Ashikin Ismail, Nazrul Anuar Nayan, Rosmina Jaafar, and Zazilah May. 2022. Recent advances in non-invasive blood pressure monitoring and prediction using a machine learning approach. *Sensors* 22, 16 (2022), 6195.

[32] Monika Jain, Niranjan Kumar, and Sujay Deb. 2016. A multi-signal acquisition system for preventive cardiology with cuff-less BP measurement capability. In *2016 8th International Conference on Communication Systems and Networks*. IEEE, 1–6.

[33] Dong-Kyu Kim, Young-Tak Kim, Hakseung Kim, and Dong-Joo Kim. 2022. Deepcnap: A deep learning approach for continuous noninvasive arterial blood pressure monitoring using photoplethysmography. *IEEE Journal of Biomedical and Health Informatics* 26, 8 (2022), 3697–3707.

[34] Ho Jong KiM, Hyeon Chul Lee, Chul Han Kim, Yun Jin Kim, and Gye Rok Jeon. 2004. Blood flow and pressure in a brachial artery under cuff pressure. In *30th Annual Conference of IEEE Industrial Electronics Society*, Vol. 3. IEEE, 2973–2977.

[35] Serkan Kiranyaz, Turker Ince, and Moncef Gabbouj. 2015. Real-time patient-specific ECG classification by 1-D convolutional neural networks. *IEEE transactions on biomedical engineering* 63, 3 (2015), 664–675.

[36] Fred Kusumoto. 2020. *ECG interpretation: from pathophysiology to clinical application*. Springer Nature.

[37] Ella Lan. 2023. Performer: A novel PPG-to-ECG reconstruction transformer for a digital biomarker of cardiovascular disease detection. In *Proceedings of the IEEE/CVF Winter Conference on Applications of Computer Vision*. 1991–1999.

[38] Tai Le, Floranne Ellington, Tao-Yi Lee, Khuong Vo, Michelle Khine, Sandeep Kumar Krishnan, Nikil Dutt, and Hung Cao. 2020. Continuous non-invasive blood pressure monitoring: a methodological review on measurement techniques. *IEEE Access* 8 (2020), 212478–212498.

[39] Yung-Hui Li, Latifa Nabila Harfiya, and Ching-Chun Chang. 2021. Featureless blood pressure estimation based on photoplethysmography signal using CNN and BiLSTM for IoT devices. *Wireless Communications and Mobile Computing* 2021 (2021), 1–10.

[40] Stephen S Lim, Theo Vos, Abraham D Flaxman, Goodarz Danaei, Kenji Shibuya, Heather Adair-Rohani, Mohammad A AlMazroa, Markus Amann, H Ross Anderson, Kathryn G Andrews, et al. 2012. A comparative risk assessment of burden of disease and injury attributable to 67 risk factors and risk factor clusters in 21 regions, 1990–2010: a systematic analysis for the Global Burden of Disease Study 2010. *The lancet* 380, 9859 (2012), 2224–2260.

[41] Mengyang Liu, Lai-Man Po, and Hong Fu. 2017. Cuffless blood pressure estimation based on photoplethysmography signal and its second derivative. *International Journal of Computer Theory and Engineering* 9, 3 (2017), 202.

[42] Sakib Mahmud, Nabil Ibtehaz, Amith Khandakar, Anas M Tahir, Tawsifur Rahman, Khandaker Reajul Islam, Md Shafayet Hossain, M Sohel Rahman, Farayi Musharavati, Mohamed Arselene Ayari, et al. 2022. A shallow U-Net architecture for reliably predicting blood pressure (BP) from photoplethysmogram (PPG) and electrocardiogram (ECG) signals. *Sensors* 22, 3 (2022), 919.

[43] Dominique Makowski, Tam Pham, Zen J Lau, Jan C Brammer, François Lespinasse, Hung Pham, Christopher Schölzel, and SH Annabel Chen. 2021. NeuroKit2: A Python toolbox for neurophysiological signal processing. *Behavior research methods* (2021), 1–8.

[44] Milad Asgari Mehrabadi, Seyed Amir Hossein Aqajari, Amir Hosein Afandizadeh Zargari, Nikil Dutt, and Amir M Rahmani. 2022. Novel blood pressure waveform reconstruction from photoplethysmography using cycle generative adversarial networks. In *2022 44th Annual International Conference of the IEEE Engineering in Medicine & Biology Society*. IEEE, 1906–1909.

[45] Philip Mehrgardt, Matloob Khushi, Simon Poon, and Anusha Withana. 2022. Pulse transit time PPG dataset. *PhysioNet* 10 (2022), e215–e220.

[46] Agnes S Meidert and Bernd Saugel. 2018. Techniques for non-invasive monitoring of arterial blood pressure. *Frontiers in medicine* 4 (2018), 231.

[47] Akiyo Misawa, Arata Suzuki, and Hirokazu Miura. 2022. Relationship analysis between BCG features and blood pressure. In *2022 Joint 12th International Conference on Soft Computing and Intelligent Systems and 23rd International Symposium on Advanced Intelligent Systems*. IEEE, 1–2.

[48] Hanlin Mou and Junsheng Yu. 2021. CNN-LSTM prediction method for blood pressure based on pulse wave. *Electronics* 10, 14 (2021), 1664.

[49] Seyedeh Somayyeh Mousavi, Mohammad Firouzmand, Mostafa Charmi, Mohammad Hemmati, Maryam Moghadam, and Yadollah Ghorbani. 2019. Blood pressure estimation from appropriate and inappropriate PPG signals using A whole-based method. *Biomedical Signal Processing and Control* 47 (2019), 196–206.

[50] Ramakrishna Mukkamala, Jin-Oh Hahn, Omer T Inan, Lalit K Mestha, Chang-Sei Kim, Hakan Töreyin, and Survi Kyal. 2015. Toward ubiquitous blood pressure monitoring via pulse transit time: theory and practice. *IEEE transactions on biomedical engineering* 62, 8 (2015), 1879–1901.

[51] Jonathan Myers, Staffan Ahnve, Victor Froelicher, and Michael Sullivan. 1985. Spatial R wave amplitude changes during exercise: relation with left ventricular ischemia and function. *Journal of the American College of Cardiology* 6, 3 (1985), 603–608.

[52] Su A Noh, Hwang-Soo Kim, Si-Hyuck Kang, Chang-Hwan Yoon, Tae-Jin Youn, and In-Ho Chae. 2024. History and evolution of blood pressure measurement. *Clinical Hypertension* 30, 1 (2024), 9.

[53] JM Padilla, EJ Berjano, J Saiz, L Facila, P Diaz, and S Merce. 2006. Assessment of relationships between blood pressure, pulse wave velocity and digital volume pulse. In *2006 Computers in Cardiology*. IEEE, 893–896.

[54] Jiapu Pan and Willis J Tompkins. 1985. A real-time QRS detection algorithm. *IEEE transactions on biomedical engineering* 3 (1985), 230–236.

[55] EK Park, BH Cho, SH Park, JY Lee, JS Lee, IY Kim, and Sun I Kim. 2006. Continuous measurement of systolic blood pressure using the PTT and other parameters. In *2005 IEEE Engineering in Medicine and Biology 27th Annual Conference*. IEEE, 3555–3558.

[56] Yaw Amofa Peprah, Ji Young Lee, and Stephen D Persell. 2023. Validation testing of five home blood pressure monitoring devices for the upper arm according to the ISO 81060-2: 2018/AMD 1: 2020 protocol. *Journal of human hypertension* 37, 2 (2023), 134–140.

[57] Philips. 2023. *Future-Focused Monitoring*. Accessed: June 25, 2023.

[58] Shital L Pingale. 2014. Using Pan Tompkin 'S Method, ECG signal processing and dignose various diseases in Matlab. In *Proceedings of IRF international conference*. 57–61.

[59] Attila Reiss, Ina Indlekofer, Philip Schmidt, and Kristof Van Laerhoven. 2019. Deep PPG: Large-scale heart rate estimation with convolutional neural networks. *Sensors* 19, 14 (2019), 3079.

[60] Alexander Reshetnik, Christopher Gohlisch, Markus Tölle, Walter Zidek, and Markus Van Der Giet. 2017. Oscillometric assessment of arterial stiffness in everyday clinical practice. *Hypertension Research* 40, 2 (2017), 140–145.

[61] Muammar Sadrawi, Yin-Tsong Lin, Chien-Hung Lin, Bhekumuzi Mathunjwa, Shou-Zen Fan, Maysam F Abbod, and Jiann-Shing Shieh. 2020. Genetic deep convolutional autoencoder applied for generative continuous arterial blood pressure via photoplethysmography. *Sensors* 20, 14 (2020), 3829.

[62] Mohammed Saeed, Mauricio Villarroel, Andrew T Reisner, Gari Clifford, Li-Wei Lehman, George Moody, Thomas Heldt, Tin H Kyaw, Benjamin Moody, and Roger G Mark. 2011. Multiparameter Intelligent Monitoring in Intensive Care II (MIMIC-II): a public-access intensive care unit database. *Critical care medicine* 39, 5 (2011), 952.

[63] Damian F Santomauro, Ana M Mantilla Herrera, Jamileh Shadid, Peng Zheng, Charlie Ashbaugh, David M Pigott, Cristiana Abbafati, Christopher Adolph, Joanne O Amlag, Aleksandr Y Aravkin, et al. 2021. Global prevalence and burden of depressive and anxiety disorders in 204 countries and territories in 2020 due to the COVID-19 pandemic. *The Lancet* 398, 10312 (2021), 1700–1712.

[64] Pritam Sarkar and Ali Etemad. 2020. Self-supervised ECG representation learning for emotion recognition. *IEEE Transactions on Affective Computing* 13, 3 (2020), 1541–1554.

[65] Pritam Sarkar and Ali Etemad. 2021. Cardiogan: Attentive generative adversarial network with dual discriminators for synthesis of ECG from PPG. In *Proceedings of the AAAI Conference on Artificial Intelligence*, Vol. 35. 488–496.

[66] Qijia Shao, Jiting Liu, Emily Bejerano, Ho Man Colman, Jingping Nie, Xiaofan Jiang, and Xia Zhou. 2024. Joey: Supporting Kangaroo Mother Care with Computational Fabrics. In *Proceedings of the 22nd Annual International Conference on Mobile Systems, Applications and Services*. 237–251.

[67] Hangsik Shin and Se Dong Min. 2017. Feasibility study for the non-invasive blood pressure estimation based on PPG morphology: Normotensive subject study. *Biomedical engineering online* 16 (2017), 1–14.

[68] Jae Hyuk Shin and Kwang Suk Park. 2012. HRV analysis and blood pressure monitoring on weighing scale using BCG. In *2012 Annual International Conference of the IEEE Engineering in Medicine and Biology Society*. IEEE, 3789–3792.

[69] Debaditya Shome, Pritam Sarkar, and Ali Etemad. 2024. Region-Disentangled Diffusion Model for High-Fidelity PPG-to-ECG Translation. In *Proceedings of the AAAI conference on artificial intelligence*, Vol. 38. 15009–15019.

[70] Revati Shriram, Asmita Wakankar, Nivedita Daimiwal, and Dipali Ramdasi. 2010. Continuous cuffless blood pressure monitoring based on PTT. In *2010 International Conference on Bioinformatics and Biomedical Technology*. IEEE, 51–55.

[71] Sima Siami-Namini, Neda Tavakoli, and Akbar Siami Namin. 2019. The performance of LSTM and BiLSTM in forecasting time series. In *2019 IEEE International conference on big data*. IEEE, 3285–3292.

[72] Monika Simjanoska, Martin Gjoreski, Matjaž Gams, and Ana Madevska Bogdanova. 2018. Non-invasive blood pressure estimation from ECG using machine learning techniques. *Sensors* 18, 4 (2018), 1160.

[73] Jascha Sohl-Dickstein, Eric Weiss, Niru Maheswaranathan, and Surya Ganguli. 2015. Deep unsupervised learning using nonequilibrium thermodynamics. In *International conference on machine learning*. PMLR, 2256–2265.

[74] Josep Solà, Martin Proença, and Olivier Chételat. 2013. Wearable PWV technologies to measure blood pressure: eliminating brachial cuffs. In *2013 35th Annual International Conference of the IEEE Engineering in Medicine and Biology Society*. IEEE, 4098–4101.

[75] Xin Tian, Qiang Zhu, Yuenan Li, and Min Wu. 2020. Cross-domain joint dictionary learning for ECG reconstruction from PPG. In *ICASSP 2020-2020 IEEE International Conference on Acoustics, Speech and Signal Processing*. IEEE, 936–940.

[76] VA Tsyrlin, MG Pliss, and NV Kuzmenko. 2016. The history of blood pressure measurement: From Hales to our days. *Arter. Gipertenz* 22 (2016), 144–152.

[77] Mauro Ursino and Cristina Cristalli. 1995. Mathematical modeling of noninvasive blood pressure estimation techniques—part I: pressure transmission across the arm tissue. *Journal of biomechanical engineering* 117 (1995), 107–116.

[78] Mario Verdugo-Marchese, Stefano Coiro, Christine Selton-Suty, Masatake Kobayashi, Erwan Bozec, Zohra Lamiral, Clément Venner, Faiez Zannad, Patrick Rossignol, Nicolas Girerd, et al. 2020. Left ventricular myocardial deformation pattern, mechanical dispersion, and their relation with electrocardiogram markers in the large population-based STANISLAS cohort: insights into electromechanical coupling. *European Heart Journal-Cardiovascular Imaging* 21, 11 (2020), 1237–1245.

[79] Annina S Vischer and Thilo Burkard. 2017. Principles of Blood Pressure Measurement–Current Techniques, Office vs Ambulatory Blood Pressure Measurement. *Hypertension: from basic research to clinical practice* (2017), 85–96.

[80] Khuong Vo, Emad Kasaeyan Naeini, Amir Naderi, Daniel Jilani, Amir M Rahmani, Nikil Dutt, and Hung Cao. 2021. P2E-WGAN: ECG waveform synthesis from PPG with conditional wasserstein generative adversarial networks. In *Proceedings of the 36th Annual ACM Symposium on Applied Computing*. 1030–1036.

[81] Guoxing Wang, Mohamed Atef, and Yong Lian. 2018. Towards a continuous non-invasive cuffless blood pressure monitoring system using PPG: Systems and circuits review. *IEEE Circuits and systems magazine* 18, 3 (2018), 6–26.

[82] Huatao Xu, Pengfei Zhou, Rui Tan, and Mo Li. 2023. Practically Adopting Human Activity Recognition. In *Proceedings of the 29th Annual International Conference on Mobile Computing and Networking* (Madrid, Spain) *(ACM MobiCom '23)*. Association for Computing Machinery, Article 85, 15 pages.

[83] Huatao Xu, Pengfei Zhou, Rui Tan, Mo Li, and Guobin Shen. 2021. LIMU-BERT: Unleashing the Potential of Unlabeled Data for IMU Sensing Applications. In *Proceedings of the 19th ACM Conference on Embedded Networked Sensor Systems* (Coimbra, Portugal) *(SenSys '21)*. Association for Computing Machinery, 220–233.

[84] Qi Ye, Bingo Wing-Kuen Ling, Nuo Xu, Yuxin Lin, and Lingyue Hu. 2021. Multimodel fusion of classifiers for blood pressure estimation. *IET Systems Biology* 15, 6 (2021), 184–191.

[85] Pengfei Zhou, Mo Li, and Guobin Shen. 2014. Use it free: instantly knowing your phone attitude. In *Proceedings of the 20th Annual International Conference on Mobile Computing and Networking* (Maui, Hawaii, USA) *(MobiCom '14)*. Association for Computing Machinery, 605–616.

[86] Pengfei Zhou, Yuanqing Zheng, Zhenjiang Li, Mo Li, and Guobin Shen. 2012. IODetector: a generic service for indoor outdoor detection. In *Proceedings of the 10th ACM Conference on Embedded Network Sensor Systems* (Toronto, Ontario, Canada) *(SenSys '12)*. Association for Computing Machinery, 113–126.

[87] Qiang Zhu, Xin Tian, Chau-Wai Wong, and Min Wu. 2021. Learning your heart actions from pulse: ECG waveform reconstruction from PPG. *IEEE Internet of Things Journal* 8, 23 (2021), 16734–16748.